nature energy

Article

https://doi.org/10.1038/s41560-023-01250-7

Inorganic wide-bandgap perovskite subcells with dipole bridge for all-perovskite tandems

Received: 1 October 2022

Accepted: 15 March 2023

Published online: 13 April 2023

Check for updates

Tiantian Li[1,2,6], Jian Xu[3,6], Renxing Lin[1], Sam Teale[3], Hongjiang Li[1], Zhou Liu[1], Chenyang Duan[1], Qian Zhao[2], Ke Xiao[1], Pu Wu[1], Bin Chen[3], Sheng Jiang[4], Shaobing Xiong[4], Haowen Luo[1], Sushu Wan[5], Ludong Li[1], Qinye Bao[4], Yuxi Tian[5], Xueping Gao[2], Jin Xie[5], Edward H. Sargent[3] ✉ & Hairen Tan[1] ✉

Operating stability has become a priority issue for all-perovskite tandem solar cells. Inorganic $CsPbI_{3-x}Br_x$ perovskites, which have good photostability against halide segregation, are promising alternatives for all-perovskite tandem solar cells. However, the interface between organic transport layers and inorganic perovskite suffers from a large energetic mismatch and inhibits charge extraction compared with hybrid analogues, resulting in low open-circuit voltages and fill factors. Here we show that inserting at this interface a passivating dipole layer having high molecular polarity—a molecule that interacts strongly with both inorganic perovskite and C_{60}—reduces the energetic mismatch and accelerates the charge extraction. This strategy resulted in a power conversion efficiency (PCE) of 18.5% in wide-bandgap (WBG) devices. We report all-perovskite tandems using an inorganic WBG subcell, achieving a PCE of 25.6% (steady state 25.2%). Encapsulated tandems retain 96% of their initial performance after 1,000 h of simulated 1-sun operation at the maximum power point.

All-perovskite tandem solar cells consisting of wide-bandgap (WBG) perovskite (~1.8 eV) and narrow-bandgap (NBG) perovskite (~1.2 eV) absorber layers extend the usable range of the solar spectrum and reduce thermalization losses in single-junction solar cells[1–4]. The highest reported power conversion efficiency (PCE) of all-perovskite tandem solar cells (26.4%) (ref. 5) has exceeded the best-performing single-junction perovskite solar cells (PSCs) (25.7%) (ref. 6); however, long-term stability remains a major bottleneck for commercial application, which requires a product lifetime of approximately 20–25 years (ref. 7).

A mixed iodine–bromine WBG perovskite is required in tandems to achieve a high open-circuit voltage (V_{OC}), yet photoinstability of WBG organic–inorganic hybrid perovskites limits long-term stability[8]. Efficient tandem devices made using a hybrid WBG layer have so far maintained only >90% of initial PCE for 600 h of operation at their maximum power point (MPP)[5]. Inorganic $CsPbI_{3-x}Br_x$ perovskites exhibit increased photostability[9–11] and excellent thermal stability, so they are good candidates for WBG absorbers[12–14]. Despite this promise, the performance of all-inorganic PSCs, especially in the inverted p–i–n device structure, lags far behind organic–inorganic PSCs, a limitation dominated by low V_{OC} and fill factors (FF)[15–19], as listed in Supplementary Table 1.

We reasoned that fast crystallization with uncontrolled intermediate phases results in poor film quality for all-inorganic perovskites[20–22]. The high density of interfacial defects leads to poor contact between the $CsPbI_{3-x}Br_x$ perovskite and electron-transport layers (ETL), which demands more effective passivation strategies. Another key challenge is that WBG $CsPbI_{3-x}Br_x$ perovskite has an inferior energetic alignment

[1]National Laboratory of Solid State Microstructures, College of Engineering and Applied Sciences, Frontiers Science Center for Critical Earth Material Cycling, Nanjing University, Nanjing, China. [2]School of Materials Science and Engineering, Nankai University, Tianjin, China. [3]Department of Electrical and Computer Engineering, University of Toronto, Toronto, Ontario, Canada. [4]School of Physics and Electronic Science, East China Normal University, Shanghai, China. [5]School of Chemistry and Chemical Engineering, Nanjing University, Nanjing, China. [6]These authors contributed equally: Tiantian Li, Jian Xu. ✉e-mail: ted.sargent@utoronto.ca; hairentan@nju.edu.cn

with ETL[23,24], especially for C_{60} that is commonly used in the inverted architecture[16,25]. Inorganic perovskites typically have higher conduction band minimums (CBM) than the equivalent hybrid perovskite at the same bandgap[26–28]. The large conduction band offset (ΔEc ≈ 0.7 eV) at this interface not only severely hinders charge extraction and leads to large V_{OC} losses[29–31] but also triggers the hysteresis in the response of current density–voltage (*J*–*V*) curves[32]. Molecules with a π-conjugated backbone have the potential to passivate trap states and facilitate charge transfer[33–36]. Organic passivators with an asymmetric structure can induce an intramolecular dipole moment across an interface owing to the unequal electronegativity.

In this Article, we find that introducing a dipole layer with high molecular polarity at the perovskite/C_{60} interface reconfigures interfacial states to improve band alignment and increase the binding between inorganic perovskite and organic contacts. This strategy enables a PCE of 18.5% with a V_{OC} of 1.23 V and average FF > 0.83 and an operational stability for over 2,000 h without PCE degradation under 1-sun illumination in WBG PSCs. Using this all-inorganic WBG subcell, we report all-perovskite tandem solar cells with a PCE of 25.6%. Encapsulated tandem devices exhibit promising operating stability, maintaining 96% of their initial performance after over 1,000 h operation at MPP.

Molecular structure design strategy

Here we pursued a π-conjugated molecular structure to insert into perovskite/C_{60} interface (Fig. 1a). Starting with the commonly used passivant phenethylammonium (PEA) cations, we seek to regulate the electric dipole moment by introducing either F atom (4-Fluorophenethylammonium (F-PEA)) or CF3 group (4-(Trifluoromethyl) phenethylammonium (CF3-PEA)) at the para position of the amino group (Fig. 1b and Supplementary Fig. 1). For this type of ammonium ligand, their $-NH_3^+$ side tends to interact with the perovskite surface[37,38], while the other side interacts with the C_{60} contact layer. The maximum electrostatic potential (φ_{max}) at the $-NH_3^+$ side of each ligand is such that: $\varphi_{max,PEA} < \varphi_{max,F\text{-}PEA} < \varphi_{max,CF3\text{-}PEA}$; while the minimum electrostatic potential (φ_{min}) at the other side is: $\varphi_{min,PEA} > \varphi_{min,F\text{-}PEA} > \varphi_{min,CF3\text{-}PEA}$. We posited that the higher φ_{max} could increase the binding strength between the inorganic perovskite and passivator and that the lower φ_{min} could increase the binding strength between ETL and passivated perovskite layers. The large difference between φ_{max} and φ_{min} within a ligand usually suggests high molecular polarity. We found that the dipole moments for the neutral molecules increase as the number of electron-withdrawing F groups increases (Supplementary Table 2).

We carried out density functional theory (DFT) calculations to understand how the molecular structure of each passivator affects defect passivation and charge transport at the perovskite/ETL interface. Among the three passivation molecules, CF3-PEA binds to the perovskite most strongly by occupying the caesium vacancy site (Fig. 1c), in accordance with its highest φ_{max} when compared with PEA and F-PEA. A stronger binding with the perovskite surface suggests a more effective surface passivation because defective sites are more likely to be passivated. We revealed that in-gap states induced by deep-level defects, that is I-Pb antisites, are eliminated after passivation with PEA or CF3-PEA (Supplementary Fig. 2). The DFT simulation results herein indicate that better surface passivation enabled by CF3-PEA is mainly ascribed to stronger binding with defect sites on the perovskite surface.

To study how the passivating molecules affect interfacial charge transport, we explored the interaction between the C_{60} layer and the perovskite surface and charge extraction at the perovskite/C_{60} interface. As shown in Fig. 1d, capping passivators induce notable charge redistribution. Charge accumulation within C_{60} molecules is repressed when passivated by PEA molecules and is further promoted in cases by F-PEA and CF3-PEA passivated perovskite. The adsorption energy (E_{ads}) of C_{60} on the control (bare), PEA, F-PEA and CF3-PEA passivated (110) perovskite surfaces are −0.47, −0.53, −0.57 and −0.71 eV, respectively. This indicates that the interaction between C_{60} and CF3-PEA passivated perovskite is strongest among the three passivators, which reduces device charge transfer resistance and accelerates interfacial charge transfer[39].

We used the Heyd–Scuseria–Ernzerhof (HSE) including spin-orbital coupling (SOC) method to calculate the projected density of states (PDOS) of C_{60}/perovskite heterojunction (Fig. 1e). It can be found that these passivators (PEA, F-PEA and CF3-PEA) do not introduce sub-bandgap states. The CBM of the entire heterojunction originates from C_{60} components. For the control and PEA passivated systems, the first conduction band (CB) of the perovskite component is far from the first CB of the C_{60} component. However, for the CF3-PEA passivated system, the first two CBs become much closer in energy, and thus the CBMs of C_{60} and perovskite align with each other. This indicates that electron extraction from the CF3-PEA passivated perovskite layer to the C_{60} layer is more efficient than that in the control, PEA and F-PEA passivated cases[40].

We further studied the work function (WF) changes and CBM shifts upon three passivator treatments (Supplementary Table 3 and Supplementary Table 4). We found that F-PEA and CF3-PEA exhibit an increased WF and CBM downshift compared with the bare surface, while PEA exhibits a decreased WF and CBM upshift compared with the bare surface. The WF shift originates from two contributions[41,42], the intrinsic dipole of the ligands ($\mu_{intrinsic}$) and the dipole created by the interaction between the ligands and the perovskite surface ($\mu_{interaction}$). $\mu_{intrinsic}$ and $\mu_{interaction}$ lie in opposite directions along the *z* axis of the surface slabs and thus have an opposite effect on the WF. Because PEA has a lower molecular polarity, its $\mu_{intrinsic}$ contribution was less than that of F-PEA and CF3-PEA and therefore insufficient to negate the WF decrease contributed by the $\mu_{interaction}$ term, resulting in an overall WF decrease. We thus offer that in cationic-type passivated cases, a higher molecular polarity helps to induce a WF increase and improve electron extraction.

Photovoltaic performance of $CsPbI_{3-x}Br_x$ PSCs employing dipole layers

DFT calculations indicated that CF3-PEA has the potential to provide more effective surface passivation and improved interfacial electron extraction than conventional PEA. To test this idea, we fabricated all-inorganic $CsPbI_{3-x}Br_x$ PSCs in the inverted p–i–n architecture to evaluate the effects of the three passivators on photovoltaic (PV) performance, and the preparation process is shown in Supplementary Fig. 3. The optimized concentration in isopropanol (IPA) of PEA, F-PEA and CF3-PEA were all 1.0 mol% relative to Cs^+ (Supplementary Fig. 4). Figure 2a and Table 1 compare the PV parameters of the control and passivated solar cells. Prototypical passivator PEA improved V_{OC} slightly but reduced the short-circuit current density (J_{SC}) and FF, resulting in only a slight improvement in PCE. Encouragingly, F-PEA and CF3-PEA substantially improved the V_{OC} and FF of devices without deteriorating J_{SC}.

Champion devices using CF3-PEA exhibited V_{OC} up to 1.23 V, a gain of 220 mV compared with control devices. Accompanied with a noticeable FF improvement (80.7% to 82.8%) and high J_{SC} (18.1 mA cm^{-2}), the champion CF3-PEA device achieved a high PCE of 18.5%, the highest value for inverted all-inorganic perovskite with a bandgap around 1.8 eV. The steady-state PCE of the CF3-PEA device is 18.3% (Supplementary Fig. 5), well matched with the PCE determined from *J*–*V* scans. The J_{SC} calculated from external quantum efficiency (EQE) agrees well with the value from *J*–*V* measurement (Fig. 2b). Supplementary Fig. 6 shows the PCE histogram of 120 CF3-PEA passivated devices with an average PCE of 17.3% and a narrow distribution with standard deviation of 0.49%. The hysteresis index (defined as $(PCE_{reverse} - PCE_{forward}) / PCE_{reverse} \times 100\%$) of control, PEA, F-PEA and CF3-PEA devices are 13.9%, 11.1%, 4.0% and 3.0%, respectively (Fig. 2c). The CF3-PEA device had the lowest hysteresis (PCEs of 18.5% vs 18.0% between reverse and forward scans), which is good compared with that of high-performance all-inorganic PSCs reported previously[43,44]. This we attribute to defect

https://doi.org/10.1038/s41560-023-01250-7

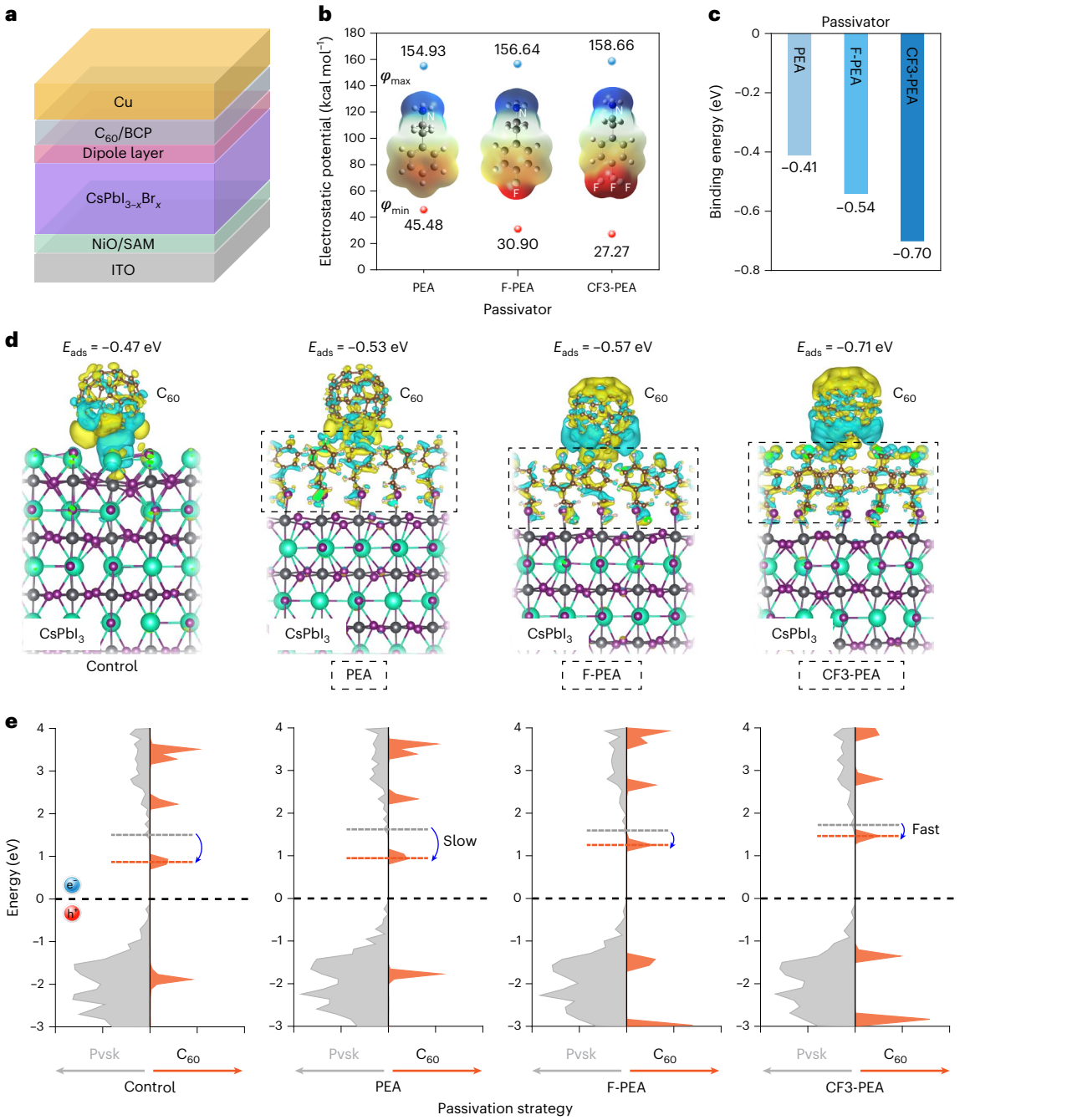

Fig. 1 | Density functional theory calculations of surface passivation and interfacial charge transport. a, Schematic structure of inverted $CsPbI_{3-x}Br_x$ PSCs. BCP, bathocuproine; SAM, self-assembled monolayer; ITO, indium tin oxide. **b**, Electrostatic potentials (φ), (φ_{max}: blue colour; φ_{min}: red colour) of each passivator (PEA, F-PEA and CF3-PEA). **c**, Binding energy between passivators and V_{Cs} defects for an Cs-I terminated (001) perovskite surface. **d**, Charge density difference (blue, depletion; yellow, accumulation) of anchoring C_{60} ETL onto the control and ammonium cation (PEA, F-PEA and CF3-PEA) passivated (110) perovskite surfaces. The same isosurface level is used. Calculated adsorption energies (E_{ads}) are also shown. The passivation molecules are shown in the dashed black box. The atoms in the structures are differentiated by different colours: Cs is represented by grass green, Pb by grey and I by purple. **e**, HSE + SOC calculated PDOS of the perovskite/C_{60} heterojunction for each passivation strategy. The grey and orange dashed lines indicate the first CB levels of perovskite and C_{60} at the interface, respectively. Pvsk: perovskite, e^-: electron, h^+: hole. The grey and orange arrows indicate the PDOS area of the perovskite layers and C_{60} layers, respectively. The blue arrow denotes the direction of electron transport at the perovskite/C_{60} interface. 'Fast' and 'Slow' labels indicate the fast/slow electron extraction property.

passivation by CF3-PEA and improved band alignment at the perovskite/C_{60} interface[45,46], a trend also seen in DFT.

We investigated the operational stability of all-inorganic $CsPbI_{3-x}Br_x$ PSCs using a multi-colour LED solar simulator with intensity equivalent to 100 mW cm^{-2} by continuously tracking the MPP in ambient conditions. The encapsulated CF3-PEA device maintained its initial PCE during 2,000 h of MPP operation (Fig. 2d). We studied the role, in achieving higher photostability, of the all-inorganic $CsPbI_{3-x}Br_x$ films vs the effect of the dipole layer. Both the control and CF3-PEA-treated devices did not show any light-induced phase segregation after 20 minutes of 10-sun equivalent illumination. In contrast, organic–inorganic hybrid perovskite films with a similar bandgap exhibited serious phase

https://doi.org/10.1038/s41560-023-01250-7

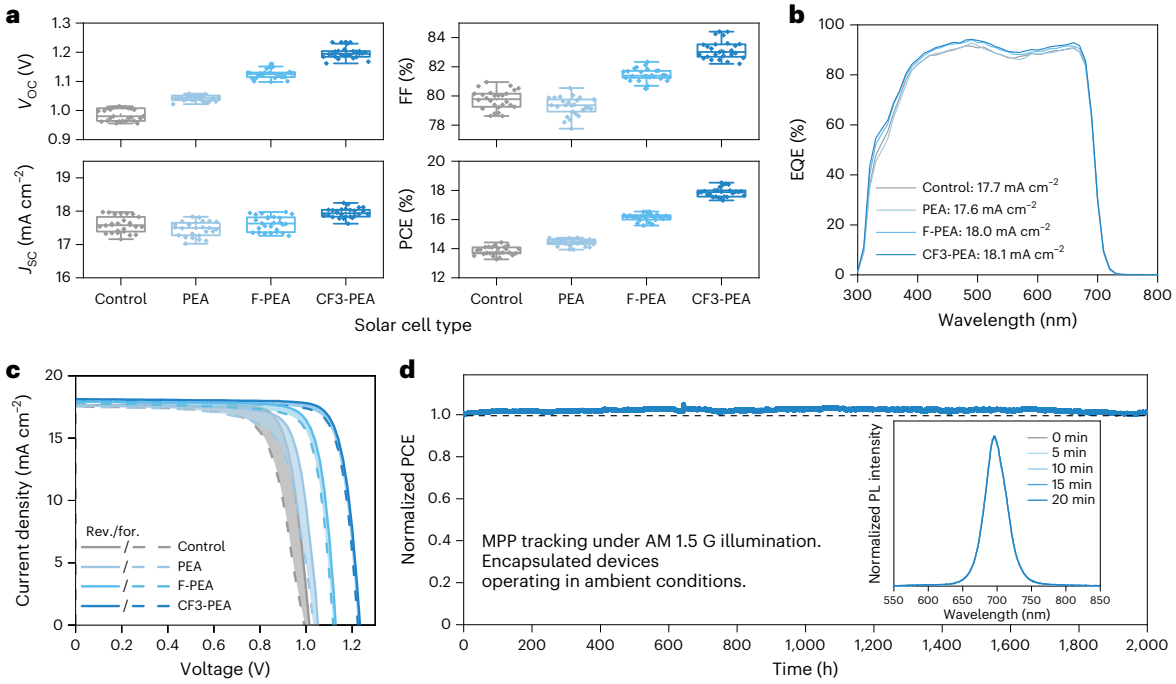

Fig. 2 | PV performance of $CsPbI_{3-x}Br_x$ perovskite solar cells with dipole layers. a, PV parameters of control and passivated solar cells (26 devices for each type). The box plot denotes median (centre line), 75th (top edge of the box) and 25th (bottom edge of the box) percentiles. The solid dots represent each device datum. **b**, EQE curves of the four champion devices. **c**, *J*–*V* curves of the four champion devices for each condition. Rev., reverse scan; for., forward scan. *J*–*V* hysteresis performance was represented by the shaded area. **d**, MPP tracking of an encapsulated CF3-PEA device for over 2,000 h in air under simulated 1-sun solar illumination (equivalent to AM1.5 G, 100 mW cm^{-2}, multi-colour light-emitting diode (LED) simulator). The device had an initial PCE of 16.8%. The operating temperature of the device was around 35 °C, and the relative humidity was approximately 30–40%. The inset shows PL spectra of CF3-PEA film under 10-sun illumination for 0, 5, 10, 15 and 20 min.

Table 1 | PV parameters of the control and passivated PSCs

Device	Scans	V_{OC} (V)	J_{SC} (mA cm^{-2})	FF (%)	PCE (%)	SPO (%)	HI (%)
Control	Reverse	1.01	17.6	80.7	14.4	13.4	13.9
	Forward	0.99	17.5	71.4	12.4		
	Average	0.99±0.02	17.6±0.24	79.7±0.64	13.8±0.29		
PEA	Reverse	1.05	17.6	79.6	14.7	13.9	11.1
	Forward	1.03	17.6	72.3	13.1		
	Average	1.04±0.01	17.5±0.22	79.3±0.62	14.4±0.23		
F-PEA	Reverse	1.13	18.0	81.7	16.5	16.1	4.0
	Forward	1.12	17.8	79.7	15.9		
	Average	1.12±0.02	17.6±0.22	81.4±0.41	16.1±0.25		
CF3-PEA	Reverse	1.23	18.1	82.8	18.5	18.3	3.0
	Forward	1.23	18.0	81.4	18.0		
	Average	1.20±0.02	18.0±0.14	83.2±0.62	17.9±0.32		

Average rows: the values represent the average and standard deviation of 26 devices under reverse scan. SPO, stabilized power output; HI, hysteresis index.

separation under identical illumination conditions (Fig. 2d inset and Supplementary Fig. 7). The inorganic PSCs also had higher thermal stability than do the organic–inorganic hybrid devices under 85 °C thermal stress (Supplementary Fig. 8 and Supplementary Fig. 9).

Characterization of $CsPbI_{3-x}Br_x$ perovskite films

Next we sought to characterize the morphology and crystalline structure of $CsPbI_{3-x}Br_x$ perovskite films to reveal the interaction between perovskites and passivators. Scanning electron microscopy (SEM) images show dense, pinhole-free control films; the morphologies of films are unchanged after passivation (Fig. 3a). Passivation treatments did not affect the overall crystallinity and no new phase was formed, as evidenced by X-ray diffraction (XRD) patterns (Fig. 3b). If the concentration of passivators increased, we found peaks at low angles ($2\theta < 10°$) appear, which correspond to diffraction signals of the original molecules (Supplementary Fig. 10). Once we used IPA to wash the high-concentration capping layers, all of these impurity XRD peaks disappeared. These results indicate that the passivators do not form 2D perovskite capping layers[47], something we assign to the strong resistance of Cs^+ to ion exchange, which is consistent with previously reported results[48,49]. The thin passivation layers also did not alter UV–vis absorption, and the band edges remain

https://doi.org/10.1038/s41560-023-01250-7

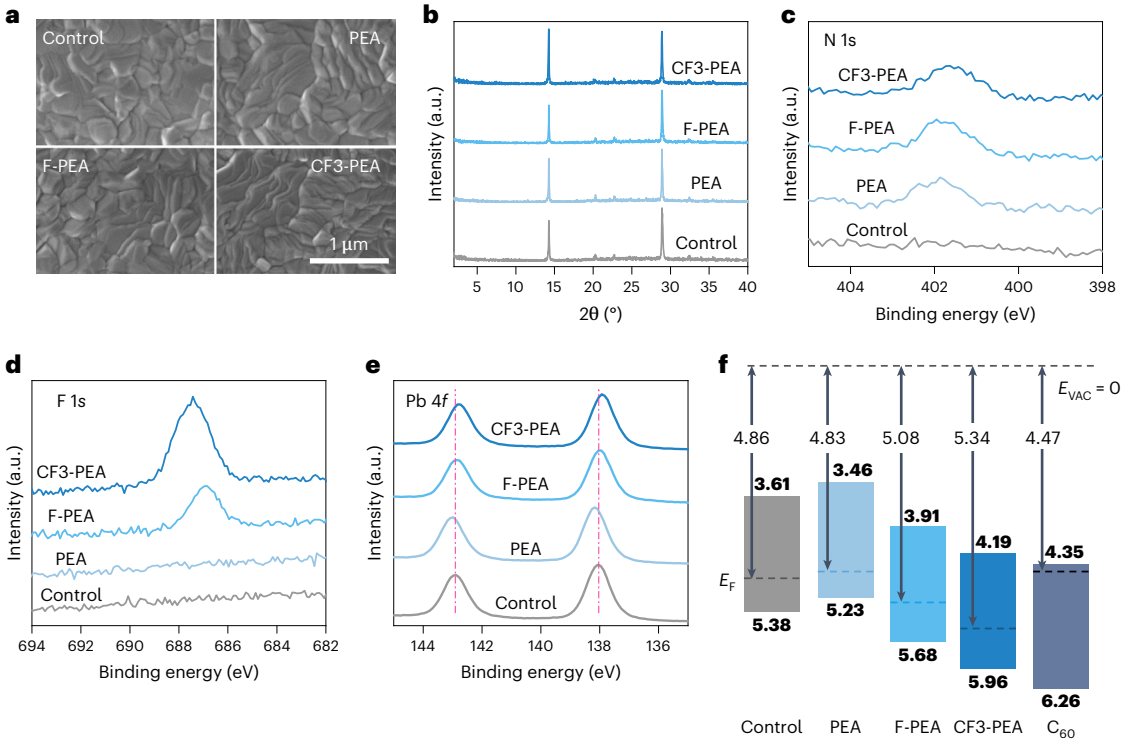

Fig. 3 | Characterization of $CsPbI_{3-x}Br_x$ perovskite films. a, SEM images of perovskite films. **b**, XRD patterns of perovskite films. **c**–**e**, XPS spectra of N 1*s* (**c**), F 1*s* (**d**) and Pb 4*f* (**e**) core level. The vertical dashed lines indicate the binding energy position of Pb 4*f* in the control film. **f**, Energy-level alignment diagram of $CsPbI_{3-x}Br_x$ and ETL. E_F: Fermi level, E_{VAC}: vacuum level. The vertical arrows indicate the work function (WF) with respect to the E_{VAC}. The horizontal dashed lines indicate the E_F in the film. The bold text: the CBMs and VBMs in the films. The regular text: the WF values.

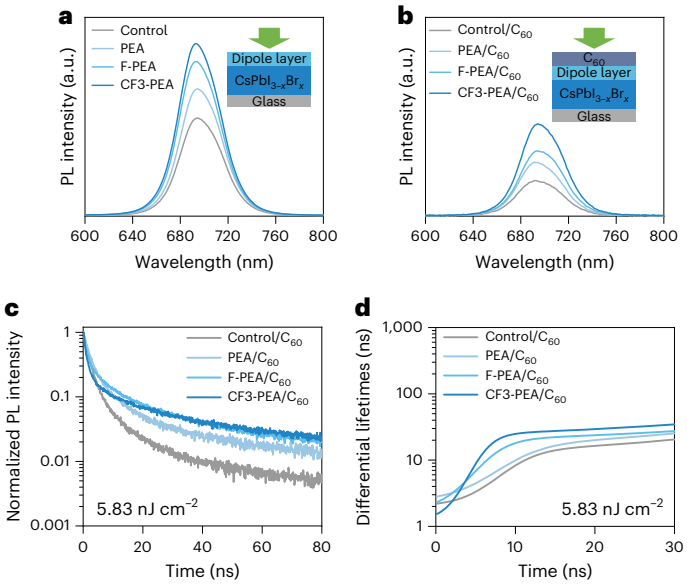

Fig. 4 | PL properties of perovskite films with different dipole layers. **a**,**b**, Steady-state PL spectra of perovskite films (**a**) and perovskite films coated with C_{60} (**b**). The insets show the sample structures and the laser illumination directions. **c**, TRPL spectra of perovskite/C_{60} junctions. **d**, Computed differential lifetimes obtained by taking the derivative from fits to the transients in **c**. The excitation fluence of TRPL spectra was 5.83 nJ cm^{-2}.

nearly unchanged (~1.77 eV) (Supplementary Fig. 11). The PV bandgap estimated from the EQE spectra is about 1.78 eV (ref. 50) (Supplementary Fig. 12), which is comparable with the optical bandgap value of 1.77 eV (Supplementary Fig. 11).

The elemental composition and electronic structure for the pristine and passivated $CsPbI_{3-x}Br_x$ films are determined by X-ray photoelectron spectroscopy (XPS) measurement. The XPS spectra of N 1*s* and F 1*s* shown in Fig. 3c,d indicate the existence of the passivator molecules on the surface of passivated films. The Pb 4*f* XPS spectrum of the control film contains two main peaks at 138.06 eV and 142.92 eV, corresponding to the Pb 4*f*7/2 and 5/2 orbitals, respectively. The Pb 4*f* peaks in the PEA passivated film shift towards higher binding energy by 0.08 eV, whereas the F-PEA and CF3-PEA passivated films shift to lower binding energies by 0.07 eV and 0.14 eV (Fig. 3e), respectively. The XPS core level spectra of Cs 3*d*, I 3*d* and Br 3*d* in perovskite are shown in Supplementary Fig. 13. The shift direction of binding energy for elements (Pb/Cs/I/Br) show the same trend, though the shift values are slightly different (Supplementary Table 5). In perovskite films with each passivator, the binding energy shift of Cs is the largest among characterized elements, indicating that the passivators have a stronger interaction with Cs[31,33].

We further performed ultraviolet photoelectron spectroscopy (UPS) to investigate the surface energetics of perovskite films and C_{60} layers (Supplementary Fig. 14 and Supplementary Fig. 15). From UPS we can see that PEA treatment decreases the WF of $CsPbI_{3-x}Br_x$ film surfaces from 4.86 to 4.83 eV with respect to the vacuum level, while F-PEA and CF3-PEA passivated films exhibit deeper WFs of 5.08 eV and 5.34 eV, respectively (Fig. 3f). The ΔEc between the CBM of $CsPbI_{3-x}Br_x$ and pure C_{60} (4.35 eV) for control, PEA-, F-PEA- and CF3-PEA-treated films are 0.74, 0.89, 0.44 and 0.16 eV, respectively. We also provide the estimated energetics of C_{60} coated on different passivation perovskite films (Supplementary Fig. 16). The energy-level alignment was presented as referenced to the vacuum level and Fermi level (E_F), respectively (Supplementary Fig. 17). We found that the PEA enlarges the ΔEc between the perovskite and C_{60}, while the F-PEA and CF3-PEA dipole layers reduce the ΔEc offset, which is consistent with the results

https://doi.org/10.1038/s41560-023-01250-7

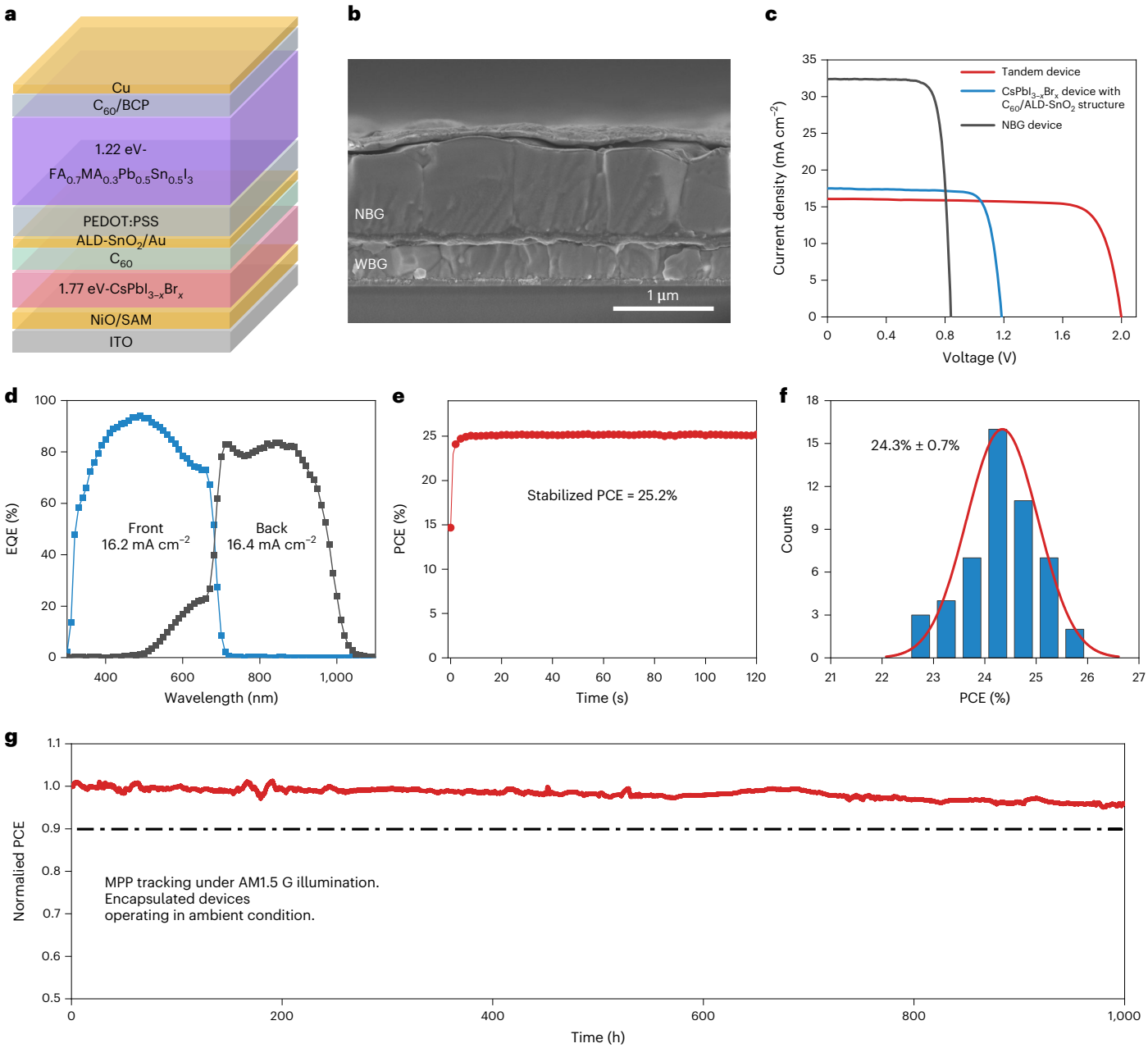

Fig. 5 | Performance of monolithic all-perovskite tandem solar cells. **a**,**b**, Schematic structure (**a**) and cross-sectional SEM image (**b**) of an all-perovskite tandem solar cell. PEDOT, PSS: poly(3,4-ethylene dioxythiophene)-poly(styrene sulfonate). **c**, The *J*–*V* measurements from a $CsPbI_{3-x}Br_x$ single-junction device with C_{60}/ALD-SnO_2 structure, a $FA_{0.7}MA_{0.3}Pb_{0.5}Sn_{0.5}I_3$ NBG device and a monolithic all-perovskite tandem cell. **d**, EQE curves of the best-performing tandem cell. **e**, Stabilized power output of the champion tandem cell. **f**, Histogram of PCEs over 50 all-perovskite tandem solar cells, showing an average PCE of 24.3 ± 0.7%. **g**, Continuous MPP tracking of an encapsulated tandem cell over 1,000 hours under simulated 1-sun illumination (equivalent to AM1.5 G, 100 mW cm^{-2}, multi-colour LED simulator) in ambient air. The device had an initial PCE of 24.1%. The operating temperature of the device was around 35 °C, and the relative humidity was approximately 30–40%.

obtained from separately measured C_{60} on top of glass/ITO. Our DFT calculations also support above experimental results of the WF changes and CBM shift upon three passivator treatments.

Drift-diffusion modelling shows that the approximately 210 mV V_{OC} increase in CF3-PEA-treated devices can be linked to a reduced energy-level mismatch between perovskite and ETL (ΔEc) and trap passivation at the perovskite surface. When we vary the surface trap density, ΔEc presents the dominant effect. The model indicates that ΔEc affects V_{OC} in two ways: increased recombination at the perovskite/C_{60} interface, which reduces quasi Fermi level splitting (QFLS), and losses purely related to band alignment where the V_{OC} is lower than the bulk QFLS (Supplementary Fig. 18).

We measured the ideality factor of devices using each treatment (Supplementary Fig. 19); values of the control, PEA, F-PEA and CF3-PEA devices were 1.32, 1.25, 1.22 and 1.17, respectively. Reduced ideality factor of devices indicates suppressed non-radiative recombination. We measured the electroluminescence spectra of control and passivated PSC devices, operating as LEDs (Supplementary Fig. 20). The CF3-PEA-passivated devices achieved significantly higher electroluminescence intensity at various applied bias. Combined with the

Table 2 | Champion PV parameters of the WBG subcell with C_{60}/ALD-SnO_2 structure, the NBG subcell and the all-perovskite tandem device

Device	V_{OC} (V)	J_{SC} (mA cm^{-2})	FF (%)	PCE (%)
WBG subcell (with ALD-SnO_2)	1.19	17.5	80.6	16.6
NBG subcell	0.84	32.4	79.7	21.7
Tandem	2.00	16.1	79.6	25.6

lowest ideality factors for the CF3-PEA passivated device, we confirm that CF3-PEA exhibits the most efficient suppression of trap-assisted recombination in devices among these three passivators.

We performed steady-state photoluminescence (PL) and time-resolved photoluminescence (TRPL) to probe the radiative recombination and carrier transfer behaviour in $CsPbI_{3-x}Br_x$ films. The passivated $CsPbI_{3-x}Br_x$ films exhibit suppressed defect-induced non-radiative recombination, as evidenced by the increased PL intensities (Fig. 4a). As shown in Fig. 4b, the CF3-PEA film coated with C_{60} shows PL enhancement, indicating the C_{60} does not induce as much recombination as it does for the control. This is due to passivation of surface defects and the band mismatch between the C_{60} and the perovskite surface. The PEA device is not worse than the control (bigger mismatch) because the QFLS of films does not decrease beyond a mismatch of approximately 0.3 eV. And then the PEA film has a lower defect density. Figure 4c presents TRPL of perovskite/C_{60} junctions, from which we calculated the differential lifetime (Fig. 4d) to distinguish charge extraction vs trap-assisted recombination. The first interval at shorter times is dominated by the transfer of electrons from the bulk into the C_{60}, and the second interval at longer delay times is dominated by interfacial recombination[51–53]. The sharp drop in emission for CF3-PEA/C_{60} indicates efficient electron transfer at the interface, and the high plateau suggests a reduced trap density. We obtained the same trend under an increased excitation fluence of 58.3 nJ cm^{-2} (Supplementary Fig. 21 and Supplementary Table 8). Drift-diffusion modelling shows that the maximum achievable J_{SC} based on absorption is 18.4 mA cm^{-2}, assuming that all absorbed photons contribute to the current (Supplementary Fig. 18d). CF3-PEA-treated devices show an average J_{SC} increase of 0.5 mA cm^{-2} compared with control devices (Supplementary Note 1).

Performance and stability of all-perovskite tandems

We then fabricated monolithic all-perovskite tandem solar cells using CF3-PEA passivated $CsPbI_{3-x}Br_x$ perovskite for the WBG subcells (Fig. 5a,b). The champion tandem device exhibited a PCE of 25.6% under reverse scan with a V_{OC} of 2.00 V, J_{SC} of 16.1 mA cm^{-2} and FF of 79.6% (Fig. 5c and Table 2). The integrated J_{SC} values of the WBG and NBG subcells from EQE spectra are 16.2 and 16.4 mA cm^{-2}, respectively, in good agreement with the J_{SC} values determined from J–V measurements (Fig. 5d). The champion tandem device exhibited a stabilized PCE of 25.2% measured over 120 s (Fig. 5e). Figure 5f shows the PCE histogram of 50 tandem solar cells processed among several batches, indicating an average PCE of 24.3% and a good reproducibility. The photovoltaic performance of tandem solar cells with all-inorganic WBG subcells is comparable to that of tandem devices with inorganic–organic hybrid WBG perovskites reported in our previous studies[54,55].

We found that the performance of $CsPbI_{3-x}Br_x$ PSCs slightly reduced in V_{OC} and FF after replacing the C_{60}/BCP-based ETL with C_{60}/ALD-SnO_2(ALD-SnO_2: SnO_2 using atomic layer deposition), required in all-perovskite tandem solar cells (Supplementary Fig. 22). The performance reduction of devices with the ALD-SnO_2 layer could be explained by the following factors: (1) the approximately 100 minute-long heating at 75 °C during ALD processing possibly altered the metastable state of the all-inorganic perovskites[56]; (2) the vacuum environment during ALD may accelerate the phase transition of all-inorganic perovskites[57]; (3) the moisture injected during water pulses could be harmful to all-inorganic perovskites, of which the phase is very sensitive to moisture[48,58].

Device stability is crucial for the commercialization of all-perovskite tandems. We investigated long-term operational stability under simulated 1-sun illumination. We tracked the power output of encapsulated devices at their MPP in ambient air under a multi-colour LED solar simulator with intensity equivalent to 100 mW cm^{-2}. The tandem devices exhibit promising operational stability and maintained 96% of initial PCE after MPP operation over 1,000 h (Fig. 5g), which is superior to the tandem devices with mixed-cation and mixed-halide hybrid WBG perovskites in previous reports[59,60].

The inorganic WBG perovskites enable a substantial advance in operating stability, yet work remains to be done to increase the PCEs of all-perovskite tandem devices. To achieve PCEs beyond 30%, the V_{OC} of the WBG front subcell must improve from 1.23 V reported here to greater than 1.4 V, something that may be obtained by further suppressing bulk and surface recombination. Regulating the rapid nucleation and crystallization process of all-inorganic perovskite films with additive and composition engineering is expected to reduce the bulk trap density. Higher V_{OC} is further expected by reducing the hole transport layer/perovskite interfacial recombination losses. Another focus will be on further improving the phase stability of WBG inorganic perovskites, something enabled by composition engineering, to avoid performance degradation in front subcells during the sequent deposition steps of the tunnel recombination junction and NBG bottom subcells. We project that by combining such efforts, it will become possible to achieve PCEs of all-perovskite tandem solar cells that reach towards those of hybrid subcells.

Conclusions

This work demonstrates efficient and stable all-perovskite tandem solar cells with an all-inorganic WBG subcell that provides improved photostability over hybrid perovskites. We demonstrate a strongly bonding electric dipole interlayer using high-polarity CF3-PEA molecules to passivate surface defects and regulate interfacial energy-level alignment, resulting in suppressed non-radiative charge recombination and improved interfacial electron extraction. Using the CF3-PEA passivator, inverted all-inorganic $CsPbI_{3-x}Br_x$ PSCs show a PCE of 18.5% with excellent operating stability over 2,000 h. We further achieve an efficiency of 25.6% (steady state 25.2%) in an all-perovskite tandem solar cell using a $CsPbI_{3-x}Br_x$ WBG subcell. The encapsulated tandem devices retain 96% of their initial performance after 1,000 h of simulated 1-sun illumination. This 1,000-h lifetime appears to surpass—by fully a factor of four times—the longest-operating lifetime reported in all-perovskite tandem cells[5]. The strategy contributes a facile route towards efficient and stable all-perovskite tandem solar cells.

Methods

First-principles calculations

First-principles calculations based on density functional theory (DFT) were carried out using the Vienna Ab initio Simulation Package[61]. For the exchange-correlation functional, the Perdew–Burke–Ernzerhof functional[62] and the screened Heyd–Scuseria–Ernzerhof (HSE) hybrid functional[63,64] were adopted. In addition, DFT-D3 method was used for the van der Waals correction[65]. The spin-orbital coupling (SOC) effect was included. The mixing parameter (α) of the Hartree–Fock term in HSE + SOC calculations was set to 0.45, which had been proven to reproduce the experimental bandgap. The plane-wave cut-off energy was 400 eV. The energy and force convergence criteria were set to 10^{-5} eV and 0.03 eV Å^{-1}, respectively. The Brillouin zone was sampled with Γ-centred k-mesh densities of $2\pi \times 0.03$ Å^{-1} in the calculations of the energetic and electronic properties. We used a vacuum of 20 Å to separate neighbouring surfaces in the z direction. The binding

energies of different ammonium cations (PEA, F-PEA and CF3-PEA) with the perovskite surface were calculated as $E_{mol/pvsk} - E_{pvsk} - E_{mol}$, where $E_{mol/pvsk}$, E_{pvsk} and E_{mol} are the total energies of the adsorption system, the perovskite system and CF3-PEAI/F-PEAI/PEAI (I represents iodide), respectively. A higher binding energy value indicates a stronger binding strength with the perovskite surface. The adsorption energies (E_{ads}) of C_{60} with different ammonium cations (PEA, F-PEA and CF3-PEA) passivated and bare perovskite surface were calculated as $E(C_{60}$@perovskite) − $E(C_{60})$ − E(perovskite). The electrostatic potentials (φ) of the passivators were calculated in the Gaussian 09 package at the B3LYP/def2TZVP level with DFT-D3. The maximum φ (φ_{max}) and minimum φ (φ_{min}) in these passivators were obtained with the help of Multiwfn code[66].

Drift-diffusion modelling for device-performance simulation

We used SCAPS-1D (a solar cell capacitance simulator) to build the device model[67]. Detailed simulation methods are illustrated in Supplementary Fig. 18 and Supplementary Tables 6 and 7.

Materials

All materials were used as received without further purification. PbI_2 (99.99%), $PbCl_2$ (99.99%), $PbBr_2$ (99.99%), 2PACz ([2-(9H-carbazol-9-yl) ethyl]phosphonic acid) (>98.0%) and MeO-2PACz ([2-(3,6-dimeth oxy-9H-carbazol-9-yl)ethyl]phosphonic acid) (>98.0%) were purchased from TCI Chemicals. SnI_2 (99.999%) was purchased from Alfa Aesar. SnF_2 (99.9%), formamidine sulfinic acid (FSA, ≥ 98%), CsI (99.999%), DMF, (99.8% anhydrous), DMSO (99.9% anhydrous), isopropanol (IPA, 99.8% anhydrous) and ethyl acetate (99.8% anhydrous) were purchased from Sigma–Aldrich. The organic halide salts (FAI, MAI, DMAI, PEAI, F-PEAI) were purchased from GreatCell Solar Materials. CF3-PEAI (99.9%) and BCP (>99% sublimed) were purchased from Xi'an Polymer Light Technology Corp. PEDOT:PSS aqueous solution (Al 4083) was purchased from Heraeus Clevios. The C_{60} was purchased from Nano-C. NiO nanocrystals were synthesized according to previous reports[68].

Perovskite precursor solution

For WBG $CsPbI_{3-x}Br_x$ perovskite, DMAI:CsI:$PbBr_2$:PbI_2:$PbCl_2$ (molar ratio = 0.9:1:0.45:0.55:0.1) were dissolved in mixed DMF and DMSO solvents (volume ratio = 1:1.4) at a concentration of 0.95 M and were stirred at 60 °C in a N_2 glovebox for 2 h before film fabrication. The precursor solution was filtered through a 0.22 μm polytetrafluoroethylene (PTFE) membrane before making the perovskite films.

For NBG $FA_{0.7}MA_{0.3}Pb_{0.5}Sn_{0.5}I_3$ perovskite, the precursor solution (2.0 M) was prepared in mixed solvents of DMF and DMSO with a volume ratio of 2:1. The molar ratios for FAI/MAI and PbI_2/SnI_2 were 0.7:0.3 and 0.5:0.5, respectively. The molar ratio of (FAI + MAI)/(PbI_2 + SnI_2) was 1:1. SnF_2 (10 mol% relative to SnI_2) was added in the precursor solution. The precursor solution was stirred at room temperature for 2 h. Tin powders (5 mg ml^{-1}) and FSA (0.3 mol%) were added in the precursor to reduce Sn^{4+} in the precursor solution. The precursor solution with the remaining tin powders was filtered through a 0.22 μm PTFE membrane before making the perovskite films.

All-inorganic perovskite solar cell fabrication

The pre-patterned ITO glass was sequentially washed with water, acetone and IPA sequentially and then treated with UV–ozone for 15 min before use. The NiO layer was spin coated onto the ITO substrate with a NiO nanocrystal suspension (20 mg ml^{-1} in water) at 3,000 r.p.m. for 30 s and subsequently annealed at 100 °C for 10 min in air. Self-assembled molecules (SAM) were used to optimize the NiO film[69]. The solutions of 2PACz and MeO-2PACz with the same concentration (0.2 mmol l^{-1} in IPA) were mixed with 1:3 ratio and then were spin coated on the NiO film at 4,000 r.p.m. for 20 s, followed by annealing at 100 °C for 5 min. After cooling, the substrates were immediately transferred to the glovebox. The perovskite precursor was spin coated on NiO/SAM at 2,600 r.p.m. for 150 s and was kept in the N_2 glovebox for 1 h before heating. The samples were then taken out from the glovebox and annealed at 170 °C for 20 min in ambient air with a humidity below 40%. For surface passivation, the passivation solution in IPA (1 mol%) was drop cast on perovskite film at 5,000 r.p.m. for 20 s, followed by drying at 90 °C for 3 min. Then the cooled films were washed by IPA at 5,000 r.p.m. for 20 s. After the cooling to room temperature, the substrates were transferred to the evaporation system. Finally, C_{60} (20 nm), BCP (7 nm) and Cu (100 nm) were sequentially deposited on top of the perovskite by thermal evaporation.

Monolithic all-perovskite tandem solar cell fabrication

The $CsPbI_{3-x}Br_x$ films were prepared as mentioned above. The substrates were transferred to the evaporation system after the fabrication of all-inorganic perovskite films, and 20-nm-thick C_{60} film was deposited on top by thermal evaporation at a rate of 0.2 Å s^{-1}. The substrates were then transferred to the atomic layer deposition (ALD) system (Veeco Savannah S200) to deposit 20 nm SnO_2 at 75 °C using precursors of tetrakis(dimethylamino) tin(IV) (99.9999%, Nanjing Ai Mou Yuan Scientific Equipment Co.) and deionized water. After ALD deposition, the substrates were transferred back to the thermal evaporation system to deposit an ultra-thin layer of Au clusters layer (~1 nm) on ALD-SnO_2. PEDOT:PSS layers were spin cast on top of front cells and annealed in air at 120 °C for 20 min. After the substrates had cooled, we immediately transferred the substrates to a nitrogen-filled glovebox for the deposition of NBG perovskite films. The perovskite films were deposited with two-step spin-coating procedures: (1) 1,000 r.p.m. for 10 s with a ramp up of 200 r.p.m. s^{-1} and (2) 4,000 r.p.m. for 40 s with a ramp up of 1,000 r.p.m. s^{-1}. Ethyl acetate (200 μl) was dropped on the spinning substrate during the second spin-coating step at 20 s before the end of the procedure. Finally, 20 nm C_{60}, 7 nm BCP and 150 nm Cu films were sequentially deposited by thermal evaporation (Beijing Technol Science). Details on the deposition of ALD-SnO_2 layers can be found in our previous work[55].

Characterization of solar cells

For single-junction solar cells, the *J*–*V* characteristics were measured using a Keithley 2400 sourcemeter under the illumination of the solar simulator (EnliTech, Class AAA) at the light intensity of 100 mW cm^{-2} as checked with National Renewable Energy Laboratory (NREL)-calibrated reference solar cells (KG-5 and KG-0 reference cells were used for the measurements of WBG and NBG solar cells, respectively). Unless otherwise stated, the *J*–*V* curves were all measured under the same conditions[70] in a nitrogen-filled glovebox with a scanning rate of 200 mV s^{-1} (voltage steps of 20 mV and a delay time of 100 ms). The active area was determined by the aperture shade mask (0.049 cm^2) placed in front of the solar cells. EQE measurements were performed in ambient air using a QE system (EnliTech) with monochromatic light focused on device pixel and a chopper frequency of 20 Hz. For tandem solar cells, the *J*–*V* characteristics were carried out under the illumination of a two-lamp high-spectral-match solar simulator (SAN-EI ELECTRIC, XHS-50S1). The spectrum from the simulator was finely tuned to ensure that spectral mismatch is within 100 ± 3% for each 50-nm interval between wavelength range 400 nm and 1,000 nm. The solar simulator was set at the light intensity of 100 mW cm^{-2} as checked with a calibrated crystalline silicon reference solar cell with a quartz window (KG-0) (detailed discussion in Supplementary Note 2). EQE measurements were performed in ambient air, and the bias illumination from highly bright LEDs with emission peaks of 850 nm and 460 nm were used for the measurements of the front and back subcells, respectively. No bias voltage was applied during the EQE measurements of tandems.

Operational stability tests of solar cells

The operating stability tests were carried out under simulated AM1.5 G illumination (Class AAA, multi-colour LED solar simulator, Guangzhou

Crysco Equipment Co.) with an intensity of 100 mW cm^{-2} using a home-built LabVIEW-based MPP tracking system and a perturb and observe method in ambient conditions (humidity of 30–50%). The solar cells were encapsulated with a cover glass and UV epoxy (Three Bond), which was cured under an UV–LED lamp (peak emission at 365 nm) for 3 min. No UV filter was applied during operation. The MPP ageing was performed at room temperature, and the device temperature was increased to around 35–40 °C during operation due to the self heating under illumination. There was no active cooling during the measurement stage. The illumination intensity was regularly calibrated to check the degradation of the LED lamp.

Other characterizations

XRD patterns were acquired using a Bruker D8 AVANTAGE Diffractometer with Cu Kα (λ = 1.54 Å) radiation. XPS analysis was carried out using the Thermo Scientific Al K-Alpha XPS system with energy steps of 0.1 eV. SEM images were obtained using a TESCAN microscope with an accelerating voltage of 2 kV. Optical absorption measurements were carried out in a Lambda 950 UV/Vis spectrophotometer.

PL measurements were conducted on a home-built wide-field microscope based on Olympus IX73. A 532 nm diode laser was used as the excitation light for the sample measurements with the laser power density on the film surface of 100 mW cm^{-2}. The fluorescence of the samples was collected by a dry objective lens (Olympus LUCPlanFI 40×, Numerical Aperture (NA) = 0.6) and detected by an Electron Multiplying Charge-Coupled Device (EMCCD) camera (iXon Ultra 888, Andor) after passing through 550 nm (ET550LP, Chroma) long-pass filters. TRPL was measured using a Horiba Fluorolog-3 time-correlated single photon counting system; the samples were excited using a pulsed laser with a wavelength of 485 nm (2 MHz, 5.83 nj cm^{-2} and 58.3 nj cm^{-2}) from the glass side. The PL decay curves were fitted with biexponential components to obtain a fast and a slow decay lifetime.

Ultraviolet photoelectron spectroscopy (UPS) was performed in an ultrahigh vacuum surface analysis system equipped with a fast entry load lock, a transfer chamber and an analysis chamber (base pressure approximately 10^{-10} mbar). UPS employed the He I 21.22 eV as the excitation source with an energy resolution of 50 meV. The work function was derived from the secondary electron cut-off and the ionization potential from the frontier edge of the occupied density states to the vacuum level. The LED device characterizations were carried out with a Keithley 2400 source meter and a 100 mm integrating sphere coupled with a spectrometer (Ocean Optics, Spectrum TEQ-EQY).

Reporting summary

Further information on research design is available in the Nature Portfolio Reporting Summary linked to this article.

Data availability

The datasets generated and analysed during the current study are included in the published article and its Supplementary Information and source data files. Source data are provided with this paper.

References

1. Chen, H. et al. Regulating surface potential maximizes voltage in all-perovskite tandems. *Nature* **613**, 676–681 (2022).
2. Wang, C. et al. A universal close-space annealing strategy towards high-quality perovskite absorbers enabling efficient all-perovskite tandem solar cells. *Nat. Energy* **7**, 744–753 (2022).
3. Tong, J. et al. Carrier control in Sn–Pb perovskites via 2D cation engineering for all-perovskite tandem solar cells with improved efficiency and stability. *Nat. Energy* **7**, 642–651 (2022).
4. Jiang, Q. et al. Compositional texture engineering for highly stable wide-bandgap perovskite solar cells. *Science* **378**, 1295–1300 (2022).
5. Lin, R. et al. All-perovskite tandem solar cells with improved grain surface passivation. *Nature* **603**, 73–78 (2022).
6. *Best Research-Cell Efficiencies* (NREL, accessed 23 January 2023); https://www.nrel.gov/pv/cell-efficiency.html
7. Wang, D., Wright, M., Elumalai, N. K. & Uddin, A. Stability of perovskite solar cells. *Sol. Energy Mater. Sol. Cells* **147**, 255–275 (2016).
8. Wen, J. et al. Steric engineering enables efficient and photostable wide-bandgap perovskites for all-perovskite tandem solar cells. *Adv. Mater.* **34**, 2110356 (2022).
9. Zhou, W. et al. Light-independent ionic transport in inorganic perovskite and ultrastable Cs-based perovskite solar cells. *J. Phys. Chem. Lett.* **8**, 4122–4128 (2017).
10. Bischak, C. G. et al. Origin of reversible photoinduced phase separation in hybrid perovskites. *Nano Lett.* **17**, 1028–1033 (2017).
11. Afsari, M., Boochani, A. & Shirdel, F. Electronic and optical properties of two propounded compound in photovoltaic applications, $CsPbI_3$ and $CH_3NH_3PbI_3$: by DFT. *Optik* **199**, 163360 (2019).
12. Balakrishna, R. G., Kobosko, S. M. & Kamat, P. V. Mixed halide perovskite solar cells. Consequence of iodide treatment on phase segregation recovery. *ACS Energy Lett.* **3**, 2267–2272 (2018).
13. Bush, K. A. et al. Compositional engineering for efficient wide band gap perovskites with improved stability to photoinduced phase segregation. *ACS Energy Lett.* **3**, 428–435 (2018).
14. Di Girolamo, D. et al. Ion migration-induced amorphization and phase segregation as a degradation mechanism in planar perovskite solar cells. *Adv. Energy Mater.* **10**, 2000310 (2020).
15. Ho-Baillie, A., Zhang, M., Lau, C. F. J., Ma, F. J. & Huang, S. Untapped potentials of inorganic metal halide perovskite solar cells. *Joule* **3**, 938–955 (2019).
16. Wang, J. et al. Highly efficient all-inorganic perovskite solar cells with suppressed non-radiative recombination by a Lewis base. *Nat. Commun.* **11**, 177 (2020).
17. Fu, S. et al. Tailoring in situ healing and stabilizing post-treatment agent for high-performance inverted $CsPbI_3$ perovskite solar cells with efficiency of 16.67%. *ACS Energy Lett.* **5**, 3314–3321 (2020).
18. Zeng, Q. et al. Polymer-passivated inorganic cesium lead mixed-halide perovskites for stable and efficient solar cells with high open-circuit voltage over 1.3 V. *Adv. Mater.* **30**, 1705393 (2018).
19. Zeng, Z. et al. In situ grain boundary functionalization for stable and efficient inorganic $CsPbI_2Br$ perovskite solar cells. *Adv. Energy Mater.* **8**, 1801050 (2018).
20. Li, T. et al. Cesium acetate-assisted crystallization for high-performance inverted $CsPbI_3$ perovskite solar cells. *Nanotechnology* **33**, 375205 (2022).
21. Wang, K. et al. Rapid nucleation and slow crystal growth of $CsPbI_3$ films aided by solvent molecular sieve for perovskite photovoltaics. *Adv. Energy Mater.* **12**, 2201274 (2022).
22. Zhang, J. et al. Molten-salt-assisted $CsPbI_3$ perovskite crystallization for nearly 20%-efficiency solar cells. *Adv. Mater.* **33**, 2103770 (2021).
23. Jiang, Q. et al. Enhanced electron extraction using SnO_2 for high-efficiency planar-structure $HC(NH_2)_2PbI_3$-based perovskite solar cells. *Nat. Energy* **2**, 16177 (2017).
24. Ye, Q. et al. Cesium lead inorganic solar cell with efficiency beyond 18% via reduced charge recombination. *Adv. Mater.* **31**, 1905143 (2019).
25. Liu, C. et al. Tailoring C_{60} for efficient inorganic $CsPbI_2Br$ perovskite solar cells and modules. *Adv. Mater.* **32**, 1907361 (2020).
26. Chang, X. et al. Printable $CsPbI_3$ perovskite solar cells with PCE of 19% via an additive strategy. *Adv. Mater.* **32**, 2001243 (2020).

27. Cho, A. N. & Park, N. G. Impact of interfacial layers in perovskite solar cells. *ChemSusChem* **10**, 3687–3704 (2017).
28. Wang, Y. et al. Thermodynamically stabilized β-$CsPbI_3$-based perovskite solar cells with efficiencies >18%. *Science* **365**, 591–595 (2019).
29. Xu, W. et al. Minimizing voltage loss in efficient all-inorganic $CsPbI_2Br$ perovskite solar cells through energy level alignment. *ACS Energy Lett.* **4**, 2491–2499 (2019).
30. Wang, H., Yuan, J., Xi, J., Du, J. & Tian, J. Multiple-function surface engineering of SnO_2 nanoparticles to achieve efficient perovskite solar cells. *J. Phys. Chem. Lett.* **12**, 9142–9148 (2021).
31. Liu, J. et al. Efficient and stable perovskite-silicon tandem solar cells through contact displacement by MgF_x. *Science* **377**, 302–306 (2022).
32. Luo, D., Li, X., Dumont, A., Yu, H. & Lu, Z. H. Recent progress on perovskite surfaces and interfaces in optoelectronic devices. *Adv. Mater.* **33**, 2006004 (2021).
33. Duan, J. et al. Effect of side-group-regulated dipolar passivating molecules on $CsPbBr_3$ perovskite solar cells. *ACS Energy Lett.* **6**, 2336–2342 (2021).
34. Tan, S. et al. Effect of high dipole moment cation on layered 2D organic–inorganic halide perovskite solar cells. *Adv. Energy Mater.* **9**, 1803024 (2019).
35. Xue, J. et al. Reconfiguring the band-edge states of photovoltaic perovskites by conjugated organic cations. *Science* **371**, 636–640 (2021).
36. Lin, Y. et al. π-conjugated Lewis base: efficient trap-passivation and charge-extraction for hybrid perovskite solar cells. *Adv. Mater.* **29**, 1604545 (2017).
37. Chen, B., Rudd, P. N., Yang, S., Yuan, Y. & Huang, J. Imperfections and their passivation in halide perovskite solar cells. *Chem. Soc. Rev.* **48**, 3842–3867 (2019).
38. Gao, F., Zhao, Y., Zhang, X. & You, J. Recent progresses on defect passivation toward efficient perovskite solar cells. *Adv. Energy Mater.* **10**, 1902650 (2020).
39. Li, B. et al. Anchoring fullerene onto perovskite film via grafting pyridine toward enhanced electron transport in high-efficiency solar cells. *ACS Appl. Mater. Interfaces* **10**, 32471–32482 (2018).
40. Liu, X. Y. et al. Spin-orbit coupling accelerates the photoinduced interfacial electron transfer in a fullerene-based perovskite heterojunction. *J. Phys. Chem. Lett.* **12**, 1131–1137 (2021).
41. Canil, L. et al. Tuning halide perovskite energy levels. *Energy Environ. Sci.* **14**, 1429–1438 (2021).
42. Leung, C., Kao, L., Su, S., Feng, J. & Chan, T. Relationship between surface dipole, work function and charge transfer: some exceptions to an established rule. *Phys. Rev. B* **68**, 195408 (2003).
43. Cui, Y. et al. A versatile molten-salt induction strategy to achieve efficient $CsPbI_3$ perovskite solar cells with a high open-circuit voltage >1.2 V. *Adv. Mater.* **34**, 2205028 (2022).
44. Zhang, H. et al. Fluorine-containing passivation layer via surface chelation for inorganic perovskite solar cells. *Angew. Chem. Int. Ed.* **62**, e202216634 (2022).
45. Wang, C. et al. Understanding and eliminating hysteresis for highly efficient planar perovskite solar cells. *Adv. Energy Mater.* **7**, 1700414 (2017).
46. Beal, R. E. et al. Cesium lead halide perovskites with improved stability for tandem solar cells. *J. Phys. Chem. Lett.* **7**, 746–751 (2016).
47. Cai, Y. et al. Graded 2D/3D $(CF3\text{-}PEA)_2FA_{0.85}MA_{0.15}Pb_2I_7$/ $FA_{0.85}MA_{0.15}PbI_3$ heterojunction for stable perovskite solar cell with an efficiency over 23.0%. *J. Energy Chem.* **65**, 480–489 (2022).
48. Liu, T. et al. Modifying surface termination of $CsPbI_3$ grain boundaries by 2D perovskite layer for efficient and stable photovoltaics. *Adv. Funct. Mater.* **31**, 2009515 (2021).
49. Wang, Y. et al. Efficient α-$CsPbI_3$ photovoltaics with surface terminated organic cations. *Joule* **2**, 2065–2075 (2018).
50. Almora, O. et al. Quantifying the absorption onset in the quantum efficiency of emerging photovoltaic devices. *Adv. Energy Mater.* **11**, 2100022 (2021).
51. Krogmeier, B., Staub, F., Grabowski, D., Rau, U. & Kirchartz, T. Quantitative analysis of the transient photoluminescence of $CH_3NH_3PbI_3/PC_{61}BM$ heterojunctions by numerical simulations. *Sustain. Energy Fuels* **2**, 1027–1034 (2018).
52. Kirchartz, T., Márquez, J. A., Stolterfoht, M. & Unold, T. Photoluminescence-based characterization of halide perovskites for photovoltaics. *Adv. Energy Mater.* **10**, 1904134 (2020).
53. Al-Ashouri, A. et al. Monolithic perovskite/silicon tandem solar cell with >29% efficiency by enhanced hole extraction. *Science* **370**, 1300–1309 (2020).
54. Lin, R. et al. Monolithic all-perovskite tandem solar cells with 24.8% efficiency exploiting comproportionation to suppress Sn(II) oxidation in precursor ink. *Nat. Energy* **4**, 864–873 (2019).
55. Xiao, K. et al. All-perovskite tandem solar cells with 24.2% certified efficiency and area over 1 cm^2 using surface-anchoring zwitterionic antioxidant. *Nat. Energy* **5**, 870–880 (2020).
56. Wang, X., Wang, Y., Chen, Y., Liu, X. & Zhao, Y. Efficient and stable $CsPbI_3$ inorganic perovskite photovoltaics enabled by crystal secondary growth. *Adv. Mater.* **33**, 2103688 (2021).
57. Guo, R. et al. Degradation mechanisms of perovskite solar cells under vacuum and one atmosphere of nitrogen. *Nat. Energy* **6**, 977–986 (2021).
58. Wang, Y., Zhang, T., Kan, M. & Zhao, Y. Bifunctional stabilization of all-inorganic α-$CsPbI_3$ perovskite for 17% efficiency photovoltaics. *J. Am. Chem. Soc.* **140**, 12345–12348 (2018).
59. Gil-Escrig, L. et al. Efficient wide-bandgap mixed-cation and mixed-halide perovskite solar cells by vacuum deposition. *ACS Energy Lett.* **6**, 827–836 (2021).
60. Chen, C. et al. Interfacial engineering of a thiophene-based 2D/3D perovskite heterojunction for efficient and stable inverted wide-bandgap perovskite solar cells. *Nano Energy* **90**, 106608 (2021).
61. Kresse, G. J. F. Efficient iterative schemes for ab initio total-energy calculations using a plane-wave basis set. *J. Phys. Chem. A* **54**, 11169–11186 (1996).
62. Perdew, J. P., Burke, K. & Ernzerhof, M. Generalized gradient approximation made simple. *Phys. Rev. Lett.* **77**, 3865–3868 (1996).
63. Paier, J. et al. Screened hybrid density functionals applied to solids. *J. Chem. Phys.* **124**, 154709 (2006).
64. Heyd, J., Scuseria, G. E. & Ernzerhof, M. Hybrid functionals based on a screened Coulomb potential. *J. Chem. Phys.* **118**, 8207–8215 (2003).
65. Lee, K., Murray, É. D., Kong, L., Lundqvist, B. I. & Langreth, D. C. Higher-accuracy van der Waals density functional. *Phys. Rev. B Condens.* **82**, 081101 (2010).
66. Lu, T. & Chen, F. Multiwfn: a multifunctional wavefunction analyzer. *J. Comput. Chem.* **33**, 580–592 (2012).
67. Burgelman, M., Nollet, P. & Degrave, S. Modelling polycrystalline semiconductor solar cells. *Thin Solid Films* **361**, 527–532 (2000).
68. Han, Q. et al. Low-temperature processed inorganic hole transport layer for efficient and stable mixed Pb-Sn low-bandgap perovskite solar cells. *Sci. Bull.* **64**, 1399–1401 (2019).
69. Li, L. et al. Flexible all-perovskite tandem solar cells approaching 25% efficiency with molecule-bridged hole-selective contact. *Nat. Energy* **7**, 708–717 (2022).

70. Belisle, R. A. et al. Interpretation of inverted photocurrent transients in organic lead halide perovskite solar cells: proof of the field screening by mobile ions and determination of the space charge layer widths. *Energy Environ. Sci.* **10**, 192–204 (2017).

Acknowledgements

This work was financially supported by the National Key R&D Program of China (2022YFB4200304), National Natural Science Foundation of China (U21A2076 and 61974063), Natural Science Foundation of Jiangsu Province (BE2022021, BE2022026, BK20202008, BK20190315), the Technology Innovation Fund of Nanjing University, Fundamental Research Funds for the Central Universities (0213/14380206; 0205/14380252), Frontiers Science Center for Critical Earth Material Cycling Fund (DLTD2109) and Program for Innovative Talents and Entrepreneur in Jiangsu. The work at University of Toronto was supported by the US Department of the Navy, Office of Naval Research (N00014-20-1-2572). J. Xu acknowledges SciNet, which is funded by the Canada Foundation for Innovation under the auspices of Compute Canada, for providing the computing resources for DFT simulations.

Author contributions

H.T. conceived the idea and directed the overall project. T.L. and C.D. fabricated all the inorganic perovskite devices and conducted the characterization. J. Xu carried out the DFT simulation. S.T. performed SCAPS simulations. K.X. helped on ALD processing. R.L. and P.W. helped on the fabrication of NBG subcells. S.J., S.X. and Q.B. performed the UPS measurements. H. Li, Z.L., B.C., H. Luo, S.W., Y.T., L.L., X.G. and J. Xie helped on the material characterization. H.T. and E.H.S. supervised the work. H.T., T.L. and J. Xu wrote the draft paper, and S.T., H. Li, Q.Z., B.C., L.L., X.G. and E.H.S. improved the paper. All authors read and commented on the paper.

Competing interests

Hairen Tan is the founder, chief scientific officer and chairman of Renshine Solar Co., Ltd., a company that is commercializing perovskite PVs. The other authors declare no competing interests.

Additional information

Supplementary information The online version contains supplementary material available at https://doi.org/10.1038/s41560-023-01250-7.

Correspondence and requests for materials should be addressed to Edward H. Sargent or Hairen Tan.

Peer review information *Nature Energy* thanks Junfeng Fang and the other, anonymous, reviewer(s) for their contribution to the peer review of this work.

nature research

Corresponding author(s): Edward H. Sargent and Hairen Tan

Solar Cells Reporting Summary

Nature Research wishes to improve the reproducibility of the work that we publish. This form is intended for publication with all accepted papers reporting the characterization of photovoltaic devices and provides structure for consistency and transparency in reporting. Some list items might not apply to an individual manuscript, but all fields must be completed for clarity.

For further information on Nature Research policies, including our data availability policy, see Authors & Referees.

Experimental design

Please check: are the following details reported in the manuscript?

1. Dimensions

Area of the tested solar cells	☒ Yes ☐ No	The "Characterization of solar cells" of "Methods"
Method used to determine the device area	☒ Yes ☐ No	The "Characterization of solar cells" of "Methods"

2. Current-voltage characterization

Current density-voltage (J-V) plots in both forward and backward direction	☒ Yes ☐ No	Figure 2c
Voltage scan conditions *For instance: scan direction, speed, dwell times*	☒ Yes ☐ No	The "Characterization of solar cells" of "Methods"
Test environment *For instance: characterization temperature, in air or in glove box*	☒ Yes ☐ No	Figure captions and "Characterization of solar cells" of "Methods"
Protocol for preconditioning of the device before its characterization	☐ Yes ☒ No	These devices are tested directly without any preprocessing.
Stability of the J-V characteristic *Verified with time evolution of the maximum power point or with the photocurrent at maximum power point; see ref. 7 for details.*	☒ Yes ☐ No	Figure 5e and Supplementary Figure 5

3. Hysteresis or any other unusual behaviour

Description of the unusual behaviour observed during the characterization	☒ Yes ☐ No	Section “PV performance of CsPbI3-xBrx PSCs employing dipole layers”
Related experimental data	☒ Yes ☐ No	Figure 2c and Table 1

4. Efficiency

External quantum efficiency (EQE) or incident photons to current efficiency (IPCE)	☒ Yes ☐ No	Figure 2b and Figure 5d
A comparison between the integrated response under the standard reference spectrum and the response measure under the simulator	☒ Yes ☐ No	The integrated Jsc values from QE were consistent with Jsc values from J-V measurements.
For tandem solar cells, the bias illumination and bias voltage used for each subcell	☒ Yes ☐ No	The "Characterization of solar cells" of "Methods"

5. Calibration

Light source and reference cell or sensor used for the characterization	☒ Yes ☐ No	The "Characterization of solar cells" of "Methods"
Confirmation that the reference cell was calibrated and certified	☒ Yes ☐ No	The "Characterization of solar cells" of "Methods"

Calculation of spectral mismatch between the reference cell and the devices under test

☐ Yes
☒ No

The light spectrum used for measurements matches well with the reference silicon cell, and we did not calculate the spectral mismatch between the reference cell and the tested devices

6. Mask/aperture

Size of the mask/aperture used during testing

☒ Yes
☐ No

The "Characterization of solar cells" of "Methods"

Variation of the measured short-circuit current density with the mask/aperture area

☐ Yes
☒ No

We measured all devices with masks.

7. Performance certification

Identity of the independent certification laboratory that confirmed the photovoltaic performance

☐ Yes
☒ No

The focus of this paper is to improve the stability of tandems using an inorganic wide-bandgap subcell. In addition, the reliability of the two-lamp high spectral match solar simulator (SAN-EI ELECTRIC, XHS-50S1) has been confirmed, so the certification is not necessary for this work.

A copy of any certificate(s)
Provide in Supplementary Information

☐ Yes
☒ No

No certificate

8. Statistics

Number of solar cells tested

☒ Yes
☐ No

Stated in the manuscript.

Statistical analysis of the device performance

☒ Yes
☐ No

Stated in the manuscript.

9. Long-term stability analysis

Type of analysis, bias conditions and environmental conditions
For instance: illumination type, temperature, atmosphere humidity, encapsulation method, preconditioning temperature

☒ Yes
☐ No

The "Operational stability tests of solar cells" of "Methods"